inorganics

MDPI

Article

A Missing Member of the Anderson–Evans Family: Synthesis and Characterization of the Trimethylolmethane-Capped $\{MnMo_6O_{24}\}$ Cluster

Andreas Winter [1,2], Patrick Endres [1,2,†], Nishi Singh [1,2], Nils E. Schlörer [1,3], Helmar Görls [3], Stephan Kupfer [4] and Ulrich S. Schubert [1,2,*]

[1] Laboratory for Organic and Macromolecular Chemistry (IOMC), Friedrich Schiller University Jena, Humboldtstr. 10, 07743 Jena, Germany; andreas.winter@uni-jena.de (A.W.); patrick.endres@uni-jena.de (P.E.); nishi.singh@uni-jena.de (N.S.); nils.schloerer@uni-jena.de (N.E.S.)
[2] Center for Energy and Environmental Chemistry Jena (CEEC Jena), Friedrich Schiller University Jena, Philosophenweg 7a, 07743 Jena, Germany
[3] Institute for Inorganic and Analytical Chemistry (IAAC), Friedrich Schiller University Jena, Humboldtstr. 8, 07743 Jena, Germany; helmar.goerls@uni-jena.de
[4] Institute for Physical Chemistry (IPC), Friedrich Schiller University Jena, Helmholtzweg 4, 07743 Jena, Germany; stephan.kupfer@uni-jena.de
* Correspondence: ulrich.schubert@uni-jena.de
† Current address: evety GmbH c/o OGE, Bamlerstr. 1b, 45141 Essen, Germany.

Abstract

In this work, the synthesis and structural characterization of the smallest possible member of the family of *bis*-functionalized $\{MnMo_6O_{24}\}$ Anderson–Evans polyoxometalates (POMs) is reported. The synthesis of the title compound $TBA_3\{[HC(CH_2O)_3]_2MnMo_6O_{18}\}$ (**1**) was accomplished by using trimethylolmethane as the capping unit (TBA: tetra(*n*-butyl)ammonium, $n\text{-}B_u4N^+$). The molecular structure of the organic–inorganic POM gave rise to yet undisclosed ^{1}H-NMR features, which are discussed thoroughly. Single-crystal X-ray diffraction (XRD) analysis revealed a highly regular 3D packing of the polyoxoanions within a matrix of TBA cations. The hybrid POM is of particular interest regarding potential applications in photocatalysis (i.e., hydrogen evolution) and energy storage. Thus, the electrochemical and thermal properties of **1** are also analyzed.

Keywords: crystal structure; hybrid materials; metal–oxygen clusters; NMR spectroscopy; polyoxometalates

check for updates

Academic Editors: Shenzhen Chang, Yaru Gong and Yanhong Chen

Received: 21 May 2025
Revised: 20 June 2025
Accepted: 8 July 2025
Published: 29 July 2025

Citation: Winter, A.; Endres, P.; Singh, N.; Schlörer, N.E.; Görls, H.; Kupfer, S.; Schubert, U.S. A Missing Member of the Anderson–Evans Family: Synthesis and Characterization of the Trimethylolmethane-Capped $\{MnMo_6O_{24}\}$ Cluster. *Inorganics* **2025**, *13*, 254. https://doi.org/10.3390/inorganics13080254

Copyright: © 2025 by the authors. Licensee MDPI, Basel, Switzerland. This article is an open access article distributed under the terms and conditions of the Creative Commons Attribution (CC BY) license (https://creativecommons.org/licenses/by/4.0/).

1. Introduction

Inorganic–organic hybrid materials composed of inorganic, molecular clusters, i.e., polyoxometalate (POM) cores, and organic ligands have attracted enormous interest since Keggin's pioneering report of the molecular structure of 12-phosphotungstic acid [1]. Over the last decades, the remarkable properties of hybrid POMs have already been utilized in various fields of application: catalysis, biomedicine, electrochemistry, photochromism, magnetism, etc. [2–4]. Thereby, the organic ligands can be coordinated with the POM via non-covalent forces [e.g., electrostatic, Van der Waals, and hydrogen-bonding (*H*-bonding) interactions] or covalent bonds. These systems are commonly referred to as class-I and class-II hybrid POMs, respectively. From the wide range of POM architectures, only a handful of polyoxoanions are commonly used for the formation of class-II compounds: the Lindqvist $[M_6O_{19}]^{q-}$, Keggin $[XM_{12}O_{40}]^{q-}$, Wells–Dawson $[X_2M_{18}O_{62}]^{q-}$, and Anderson–Evans

$[M_6XO_{24}]^{q-}$ polyoxoanions [5]. The synthesis of these hybrid POMs typically starts from simple inorganic materials (e.g., VO_4^{3-}, MoO_4^{2-}, WO_4^{2-}, etc.), which—depending on the applied reaction conditions—afford lacunary structures to which organic or organometallic ligands can be grafted. Alternatively, the in-situ formation of POMs in the presence of appropriate ligands, commonly equipped with hydroxy functionalities, yields organo-functionalized POMs. In either case, post-assembly functionalization of the hybrid POMs is enabled if appropriate functional groups are introduced via the organic ligands [5]. For example, cross-coupling reactions [6,7], esterification [8], amidation [9], Schiff-base formation [10,11], Cu-catalyzed azide-alkyne cycloaddition (CuAAC) [12], or metal-to-ligand coordination [13,14] have been inter-alia used in this context. With respect to POMs of the Anderson–Evans family, the twofold trisalkoxylation has been identified as a powerful tool to prepare hybrid POMs, in which the planar $[M_6XO_{24}]^{q-}$ moiety is symmetrically functionalized with tripodal organic ligands on both sides (the so-called δ-isomer) [15–17]. This strategy has been successfully applied to a range of commercially available triol derivatives, including $RC(CH_2OH)_3$ (R = CH_2OH, NH_2, OH, CH_3, etc.; Scheme 1), to yield Anderson–Evans-type POMs with various central heteroatoms [18]. Moreover, strategies to obtain single-side functionalized or less symmetric bis-functionalized derivatives (e.g., the χ- or β-isomers) have also been explored to a significant extent [16].

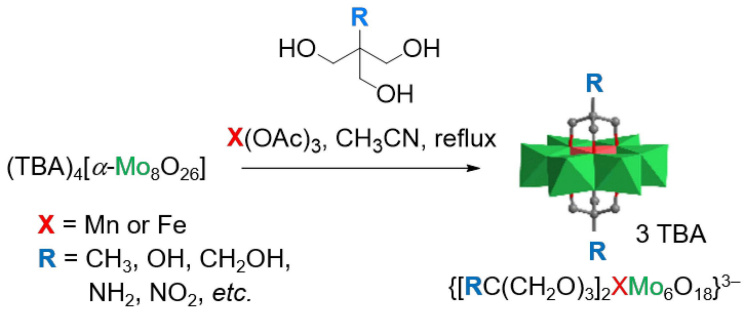

Scheme 1. Schematic representation of the synthesis of hybrid Anderson–Evans POMs via a twofold trisalkoxylation approach using tripodal triols as the organic ligands and $[\alpha\text{-}Mo_8O_{26}]^{4-}$ as the POM precursor [TBA: tetra(*n*-butyl)ammonium].

Furthermore, these molecules have been modified to obtain "functional" ligands bearing light-responsive diazo residues [19], redox-active ferrocene entities [20], or binding sites for metal-to-ligand coordination [13]. Besides the rather flexible systems, rigid triols, in which the triol anchor is directly attached to aromatic rings, have also been grafted onto the $[M_6XO_{24}]^{q-}$ unit. The aromatic systems include parent benzene [14] and pyridine [21] as well as bipyridine [14]. However, the simplest triol, 2-(hydroxymethyl)propane-1,3-diol or tris(hydroxymethyl)-methane, has largely been overlooked as a tripodal ligand for POM functionalization. Until recently, this compound was hardly commercially available [22]. Moreover, the resulting hybrid POM was considered to be of limited chemical use, since any further post-synthesis modification is restricted. The first hybrid POMs carrying this organic ligand were reported in 2019 by Wu et al. [23]. The authors prepared a series of $[Mo_6XO_{18}\{(OCH_2)_3CH\}2]^{q-}$ hybrids (X = V, Ni, Cu) and studied their solid-state structures, which depended on the nature of the counter cation and incorporated a metal center.

Against the background of finding new energy storage materials, particularly for large-scale applications, POMs have recently moved into the focus of interest [24]. Unlike conventional battery systems, the energy in redox-flow batteries (RFBs) is stored in the electrolyte, which is circulated through the cell and stored in external tanks. In order to meet the rapidly increasing needs of large-scale energy storage and improve grid reliability and utilization, low-cost, redox-stable electrolyte materials are urgently required. These

requirements are basically met by POMs, which are typically derived from earth-abundant transition-metal oxides. The first example of a POM-based RFB was proposed in 1997 [25]. As summarized recently by Lu et al., a wide range of POM systems have already been tested for RFB applications, with a strong focus on Keggin- and Dawson-type POMs [24]. Hybrid POMs from the Anderson–Evans family have not yet been used for this purpose due to the detrimentally low theoretical capacity, which results from the relatively high molar mass of the organic ligands. In order to counteract this, 2-(hydroxymethyl)propane-1,3-diol, as the smallest possible organic ligand, gains attention: Decreasing the molar mass of the organic ligands automatically gives rise to an increase in theoretical capacity as one relevant parameter in the design of active materials.

Moreover, POMs represent versatile catalysts for the hydrogen-evolution reaction (HER), which might be performed electro- or photocatalytically [26,27]. In the latter case, the POM is combined with an appropriate sensitizer, e.g., a photochemically active transition-metal complex [28,29].

Here, the synthesis and structural characterization of the hybrid POM **1** is presented. In view of the potential application in non-aqueous RFBs or the photocatalytic HER, the electrochemical properties of **1** in solution are analyzed. Whilst research in these directions is currently ongoing, we report the synthesis and detailed structural characterization of the title compound by mass spectrometry, ^{1}H-NMR spectroscopy, elemental analysis, and single-crystal/powder XRD analysis, which is supported by quantum chemical simulations.

2. Results

*2.1. Synthesis and Characterization of **1***

The synthesis of the $[\alpha\text{-}Mo_8O_{26}]^{4-}$ precursor was accomplished using the optimized procedure, which was established by Ikegami and Yagasaki [30]. Subsequently, the transformation into **1** was achieved by reacting $[\alpha\text{-}Mo_8O_{26}]^{4-}$ in the presence of $Mn(OAc)_3$ and 2-(hydroxymethyl)propane-1,3-diol. Thereby, Hasenknopf's original reaction conditions were adopted (i.e., refluxing in CH_3CN solution; Scheme 2) [31]. These authors also pointed out the necessity of having labile ligands attached to the heteroatom (e.g., acetate or acetoacetate). The fast displacement of these is known to facilitate the product formation. Orange crystals of $TBA_3\{[HC(CH_2O)_3]_2MnMo_6O_{18}\}$ (**1**) were obtained by the diffusion of diethyl ether into the reaction mixture (73% yield). The obtained material was thoroughly characterized by IR and ^{1}H-NMR spectroscopy, mass spectrometry, as well as single-crystal X-ray diffraction (scXRD) analysis. Likewise, the phenyl-equipped POM **2** was prepared via the same procedure but using 2-(hydroxymethyl)-2-phenylpropane-1,3-diol ("Ph-triol") as the organic ligand [14]. In the context of this study, **2** served as an available reference hybrid POM when discussing the electrochemical and thermal properties of **1** (see Section 2.4).

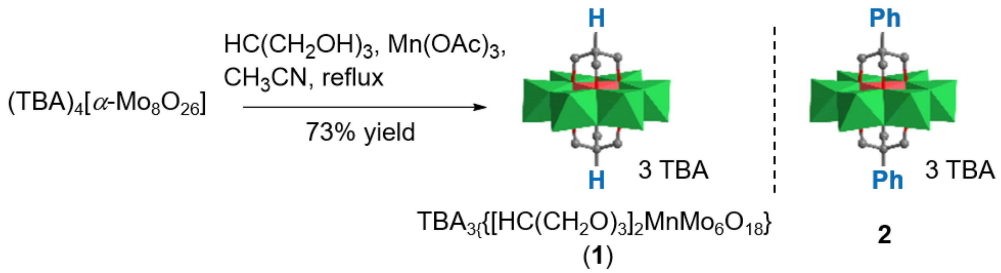

Scheme 2. Schematic representation of the synthesis of **1**. A schematic representation of the related phenyl-equipped POM **2** is also shown [14].

The FT-IR spectrum of **1** revealed the characteristic vibrational bands, which have been assigned to symmetrically functionalized Anderson–Evans POMs [31]. Following

this common assignment, the vibration of the C–O bonds appears as a relatively sharp band at ca. 1043.5 cm^{-1} (Figure S1a). The terminal Mo=O moieties gave rise to a group of intense bands in the range of ca. 950 to 875 cm^{-1}, whereas the broad vibrational band of the bridging Mo–O–Mo moieties—μ_2-O as well as μ_3-O ones—was located at ca. 650 cm^{-1}. The bands at wavenumbers >1300 cm^{-1} were assigned to vibrations of the organic ligand and the TBA cations. Moreover, the FT-IR spectra of **1** was in very good agreement with that of **2** (Figure S1b). The slight differences in peak position were attributed to the different substituents (i.e., H vs. Ph). In particular, the vibrations of the C–O bonds were shifted to a higher frequency by ca. 14 cm^{-1}, whereas the vibrational bands which were assigned to the cluster core and the TBA cations were hardly affected when changing the substituent from H to Ph.

The mass spectrometric characterization of **1** was performed by the means of MALDI-TOF MS using 9-aminoacridine (9-AA) or *trans*-2-[3-(4-*tert*-butylphenyl)-2-methyl-2-propenyliden]malononitrile (DCTB) as the matrix. The application of MALDI-TOF in the context of POM analysis is non-trivial and requires a cautions selection of the matrix and salt additive [32]. In both cases, meaningful spectra showing the identity of the title compound were obtained. Representatively, the MALDI-TOF MS of **1**, which was obtained with the 9-AA matrix, is shown in Figure 1 (the full spectrum is displayed in Figure S2). In this case, the peak at the highest m/z value has been assigned to the $[\mathbf{1} + TBA - H]^+$ species. However, when using DCTB as the matrix, the peak of the [**1** − O + DCTB]+ species represented the most prominent one (Figure S3).

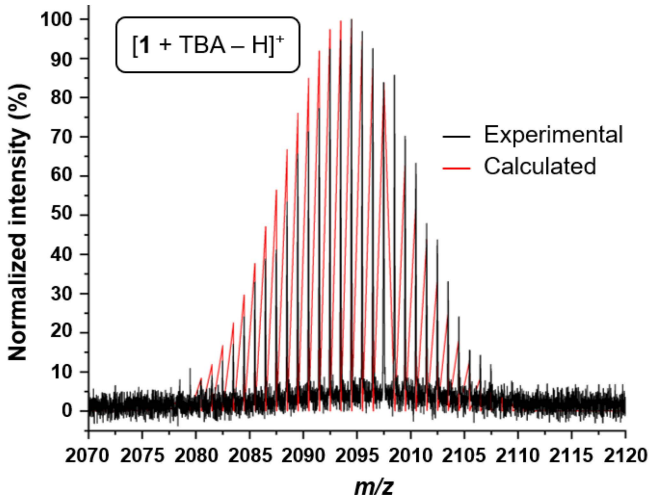

Figure 1. Experimental MALDI-TOF MS data of **1** (positive mode, matrix: 9-AA) and the corresponding calculated isotopic pattern. For clarity, only the region of the peak with the highest m/z value is shown (for the full spectrum, see Figure S2).

When analyzing the ^{1}H NMR spectra of Anderson–Evans-type POMs, one must be aware of the considerable influence of the electronic properties of the cluster on the chemical shifts. In particular, the paramagnetic Mn(III) center, present in **1**, has a tremendous impact on the chemical shift of the protons of the CH_2-groups in close proximity to the POM moiety—these protons experience a remarkable signal broadening and shift to ca. 60 ppm. Due to the chemical equivalence of the six OCH_2 groups, only one signal is observed. This feature is a characteristic of trisalkoxylated, Mn(III)-containing Anderson–Evans POMs and represents a clear indication of product formation [13]. It is commonly accepted that the more remote protons of the organic ligands (if present) are hardly affected by the paramagnetic effect and, thus, their ^{1}H NMR signals appear in the "normal" ppm range and are less broadened ("normal" signal splitting is observed if they are remote enough) [33].

In the present case, the broad signal for the CH_2O groups observed was 56.13 pm, which was more shielded compared to those cases where the neighboring carbon center was a quaternary one or equipped with an -I substituent. The second broad signal at −16.51 ppm was assigned to the CH group (Figures 2 and S4). As expected, the four signals of the TBA cations were found in the normal ppm range (Figure S5). Attempts were also made to record H–H or C–H correlation spectra in order to verify the assignment. The *T*1 values for the relaxation were determined (Table 1). However, these processes were too fast and, thus, precluded successful measurements. Further details on the measurement of the *T*1 relaxation times are provided in the Supplementary Materials (Figures S6 and S7, Table S1). The influence of the paramagnetic Mn(III) center also prevented a reliable analysis of the compound by ^{13}C-NMR spectroscopy, specifically DEPT-135—only the four signals corresponding to the carbon atoms of the TBA cations were observed under standard measurement conditions (Table 1, Figure S8).

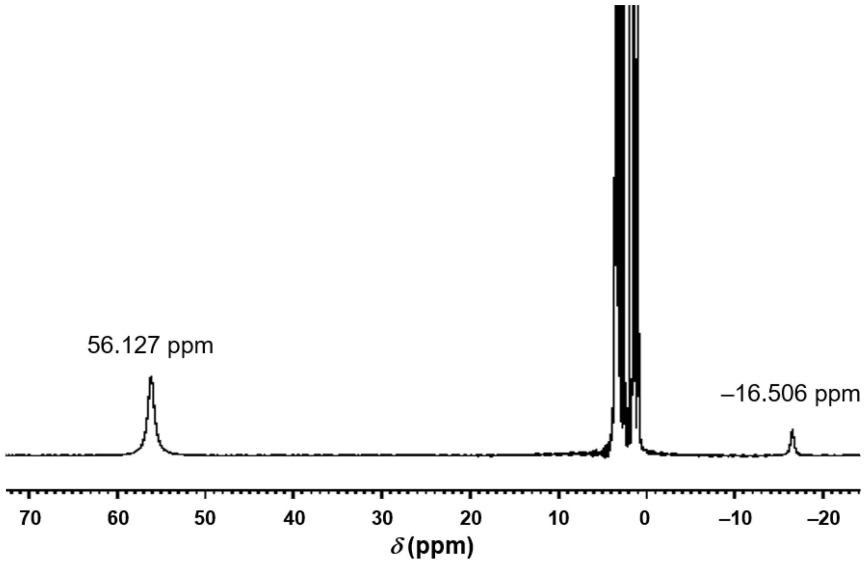

Figure 2. ^{1}H-NMR spectrum of **1** (d_6-DMSO, 500 MHz, 298 K). The cropped signals at 0 to 5 ppm are assigned to the NMR solvent, TBA cations, and residual DMAc molecules (see Figures S4 and S5).

Table 1. Summary of the ^{1}H-NMR and ^{13}C-NMR data of **1**.

	δ_H (ppm)	*T*1 (ms) [1]	δ_C (ppm)
TBA cation	3.16, 1.57, 1.31, 0.94	n/a	58.0, 23.6, 19.8, 14.2
$HC[CH_2O-]_3$	−56.13	0.99	n/a [2]
$HC[CH_2O-]_3$	−16.51	2.01	n/a [2]

[1] Details on the determination of *T*1 are provided in the Supplementary Materials (Figures S6 and S7, Table S1).
[2] The corresponding signals could not be detected in ^{13}C-NMR experiments.

Although the organic fraction of the hybrid POM was relatively small, the elemental analysis provided CHN values that were close to the theoretical ones (the best fit was obtained when taking the presence of 2.2 eq. of DMAc into account). For comparison, the ^{1}H-NMR spectroscopic analysis suggested the presence of ca. 2.1 eq. of DMAc.

2.2. X-Ray Diffraction Analysis of ***1***

Single crystals of **1**, which were suited for X-ray structure analysis, were obtained by slow diffusion of diethyl ether into the filtered DMAc reaction solutions. Details on the crystal structure parameters and the refinement are given below (Section 4.3). The POM derivative **1** crystallized in a triclinic space group Pī with *Z* = 6. As shown in

Figure 3a, **1** represents a typical example of a symmetrically disubstituted POM from the Anderson–Evans family (i.e., the *D*3-symmetric *δ*-isomer) [17]. The observed values for the Mo–O bond distances and O–Mo–O bond angles are in the typical regime as reported for such POMs (the numbering scheme of the anion's atoms is shown in Figure S9) [31]. The central Mn(III) ion is surrounded by six O-atoms in an octahedral fashion. The two tripodal organic ligands are attached to these O-atoms. The Mn–O bond lengths are in the range of 1.924(4) to 2.053(5) Å. In agreement with previous reports on the XRD analysis of Mn(III)-centered POMs, only a slight elongation of the axial Mn–O bonds of the [MnO_6] octahedron was observed; thus, Jahn−Teller distortions are largely suppressed by the rigid POM framework structure [10]. Moreover, the Mn–O bond lengths corroborate the assumption of a high-spin state of the Mn(III) center (S = 2; otherwise, the bonds would be significantly shorter) [34]. In order to verify this assumption, in-depth quantum chemical simulations were performed to evaluate the complex electronic structure of **1**, i.e., with respect to its spin state (see Section 2.3). The C–O bond lengths are in the range of 1.436(8) to 1.455(9) Å, similar to those in related POMs, such as the phenyl-modified POM **2**, which was reported earlier (Figure 2) [14]. It is thus concluded that the nature of the lateral substituent (i.e., hydrogen or phenyl) had a negligible influence on the binding of the tripodal ligand to the cluster. The crystallographic data and structure-refinement parameters for **1** are summarized in Table 2; the full list of bond lengths and angles is provided in Table S2.

Table 2. Crystallographic data and structure-refinement parameters for **1**.

	1
Formula	$3[C_{16}H_{36}N]^+$, $[C_8H_{14}MnMo_6O_{24}]^-$, 4/3($C_4H_9NO$)[+ solvent]
Formula weight	1968.30 g mol^{-1} [a]
Color	red-orange prisms
Crystal size	0.102 × 0.092 × 0.088 mm^3
Crystal system	triclinic
Space group	P ī
Unit-cell dimensions	a = 20.6350(3), b = 25.0808(3), c = 25.7043(3) Å, α = 87.564(1), β = 80.831(1), γ = 73.226(1)°
Unit-cell volume	12,574.2(3) $Å^3$
Temperature	−140(2) °C
Wavelength	0.071 nm
Z	6
Calculated density	1.560 g cm^{-3}
Absorption coefficient	10.84 cm^{-1} [a]
Absorption method	multi-scan
Absorption corr. $trans_{min/max}$	0.7044/0.7456
F(000)	6072
Measured data	92,744 reflections in h(−26/26), k(−32/32), l(−33/32)
Range	1.483° ≤ Θ ≤ 27.472°
Completeness	96.7%
Independent data/R_{int}	55,280/0.0369
Data with I > 2σ(I)	37,801
Parameters	2715
Restraints	30
wR2 (all data, on F2) [b]	0.1341
R1 (I > 2σ(I)) [b]	0.0679
s [c]	1059
Res. dens./e·$Å^{-3}$	2.764/−1.892 e $Å^{-3}$
CCDC deposition number	2226003

[a] The derived parameters do not contain the contribution of the disordered solvent. [b] Definition of the *R* indices: $R_1 = (\Sigma \| \|F_o\| - \|F_c\| \|)/\Sigma \|F_o\|$; $wR_2 = \{\Sigma[w(F_o^2 - F_c^2)^2]/\Sigma[w(F_o^2)^2]\}^{1/2}$ with $w^{-1} = \sigma^2(F_o^2) + (aP)^2 + bP$; $P = [2F_c^2 + \mathrm{Max}(F_O^2]/3$. [c] Definition of the *s* value: $s = \{\Sigma[w(F_o^2 - F_c^2)^2]/(N_o - N_p)\}^{1/2}$.

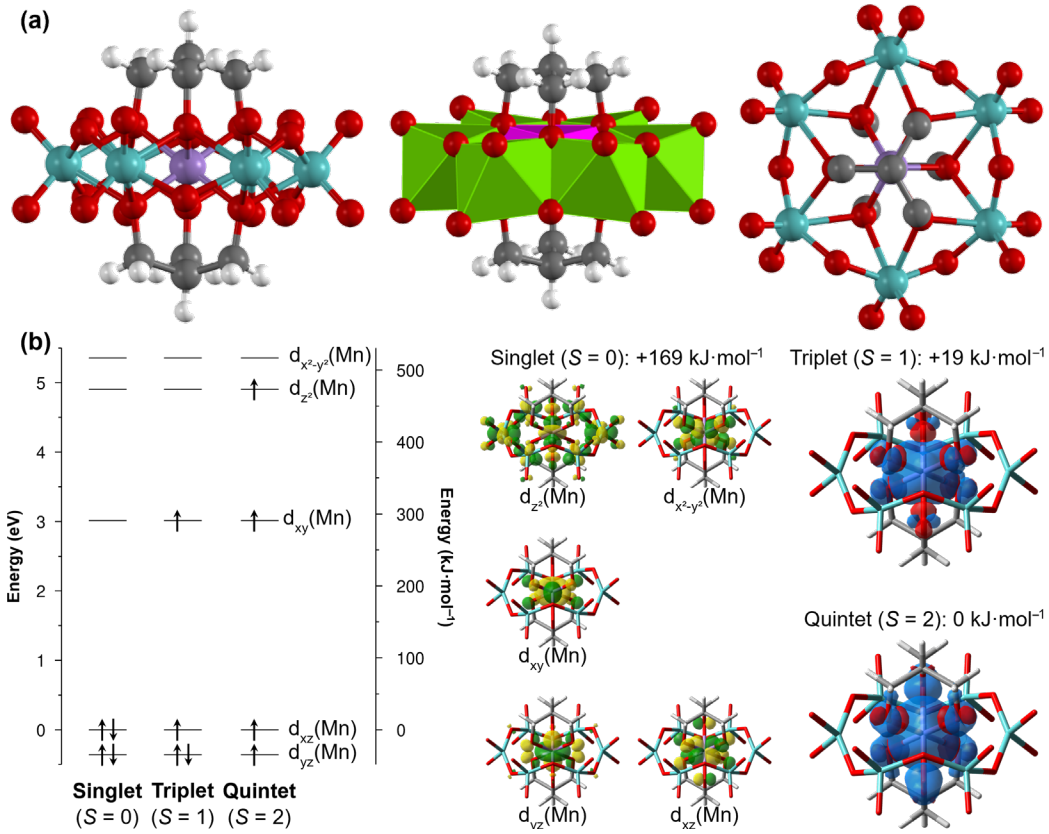

Figure 3. (**a**) X-ray molecular structure of the polyoxoanion of **1**; the TBA cations are omitted for clarity (left: side view, middle: polyhedral representation of the side view, right: top view). In the left figure, the ellipsoids represent a probability of 30%; H-atoms are drawn with arbitrary radii. In the right figure, the H-atoms are omitted for clarity. For the sake of clarity, the numbering scheme of the polyoxoanion is displayed separately in Figure S9. (**b**) Molecular frontier orbital diagram featuring the *d*-orbitals of the polyoxoanion of **1** as obtained for its closed-shell singlet configuration (B3LYP/def2-SVP, gas phase). Orbital occupations within its triplet and quintet ground states are indicated accordingly and are based on their respective spin density (visualizing unpaired electrons). Relative Gibbs free energies (T = 298 K) as obtained within their respective equilibrium structures are provided.

Due to the compact nature and the absence structure-directing substituents (e.g., aromatic moieties), the packing of **1** is fundamentally different from that of other related Anderson–Evans POMs [14,31,35]. Moreover, the packing mode is different from that reported by Wu et al. [23]. Their POMs also contained 2-(hydroxymethyl)propane-1,3-diol as the organic ligand, but due the presence of Na^+ ions, a framework structure was formed in which polyoxoanions were linked via the alkali cations. In the present case, the TBA cations separate the polyoxoanions from each other. The cations' alkyl chains form C–H···O hydrogen bonds with the $\{MnMo_6O_{24}\}$ clusters, specifically with their terminal Mo-oxo moieties (Figure S10a) [35]. In addition to this, weak *H*-bonding between the clusters and DMAc molecules, which are incorporated in the crystals, is identified (Figure S10b). The polyoxoanions are assembled into chains, in which every second anion is oriented orthogonally to the former one. The center-to-center distance between cluster anions within a chain is 12.540 Å (looking along the crystallographic *b*-direction), whereas the mean center-to-center distance of parallel chains is ca. 13.02 Å and ca. 14.50 Å. Each unit cell contains three symmetry-independent $\{MnMo_6O_{24}\}$ anions (Figure S11). The anions are surrounded by a densely packed matrix of TBA cations and DMAc solvent molecules. The

number and volume of voids are relatively small and account for only ca. 5% of the overall volume of the unit cell.

Moreover, XRD analysis was performed with a powdered sample of **1**. The thusly obtained pattern was in good agreement with the simulated one, thus confirming the phase purity of **1** (Figure S12). The intense diffraction peaks at small 2θ values are indicative of the sample's high degree-of-crystallinity. The difference in the reflection intensities between the simulated pattern and the experimental one are presumably due to different orientation of crystals in the powdered sample [36].

*2.3. Computational Studies of **1***

The electronic and structural properties of **1** were studied using computational modelling, as performed at the density functional level (DFT) of theory (see Section 4.4 for details regarding the computational setup). To this aim, three possible spin-states were considered: the closed-shell singlet ground state (S = 0; low-spin) as well as two opened-shell (high-spin) configurations, namely the triplet and quintet species with S = l and S = 2, respectively (Figure 3b). Fully relaxed equilibrium structures were obtained for all three species within the gas phase as well as within acetonitrile (i.e., in an implicit solvent environment). All optimized structures are freely available via the Zenodo online repository [37].

In the gas phase, the computational results clearly reveal that the low-spin state is energetically unfavorable and is predicted to be 169 kJ·mol^{-1} less stable in comparison to the respective quintet (high-spin) species. However, the triplet species is slightly less favorable than the quintet species (ΔG = 19 kJ·mol^{-1}). Notably, these relative Gibbs energies are obtained within the fully relaxed equilibrium structures of the respective spin states. Thereby, all three spin states formally feature a d^4 configuration of the central Mn(III) of **1**. As visualized in Figure 3b, the singlet intermediate features doubly occupied d_{xz} and d_{yz} orbitals, while in triple multiplicity, the two unpaired electrons are present—consequently leading to a $(d_{xz})^2$, $(d_{yz})^1$, $(d_{xy})^1$ scenario. Based on the rather small ligand-field splitting of the 3*d* metal and the comparably large stabilization by the exchange integral, formation of the quintet, which features four unpaired electrons, i.e., $(d_{xz})^1$, $(d_{yz})^1$, $(d_{xy})^1$, $(d_z{}^2)^1$, is preferred. To provide a more complete picture of the energetic profile of these species, we calculated the energies of all three considered spin states within each of the three equilibrium structures. The predicted electronic energies are in full agreement with the conclusions drawn from the Gibbs free energy analysis, which yields Boltzmann factors of 0, 1, and 2250 for the singlet, triplet, and quintet species (see Table S3). The preference of **1** to form a quintet high-spin species is also observed in solution (CH_3CN), while the fraction of the quintet species is 30993 : 1 : 0 in comparison to the triplet and singlet species, which are even more pronounced (see Table S4). These findings are in full agreement with the experimental findings based on the XRD structure analysis (see Section 2.2).

*2.4. Electrochemical and Thermal Properties of **1***

In order to explore the applicability of **1** to act as a hydrogen-evolution catalyst for the photocatalytic water splitting, or as active material for energy-storage applications, specifically in non-aqueous redox-flow batteries, its electrochemical properties were analyzed by cyclic voltammetry (CV) in CH_3CN solution, using $TBAPF_6$ as the conducting salt ($TBAPF_6$: tetra(*n*-butyl)ammonium hexafluorophosphate). As shown in Figure 4, the CV curve exhibited a quasi-reversible oxidation process at +0.39 V vs. Fc/Fc^+. The quasi-reversible redox at negative potential, which is commonly assigned to the Mn(II)/Mn(III) redox couple [38], exhibited the typical splitting of its oxidation peak (i.e., −0.81 V and −1.10 V) and the corresponding reduction peak at −1.31 V. For comparison, the redox processes of the POM

2 were observed at 0.22 V and −1.34 V, respectively [14]. Thus, compound 1 possessed a lower electrochemical band gap (ΔE^c) than the other compound (i.e., 1.45 eV vs. 1.56 eV).

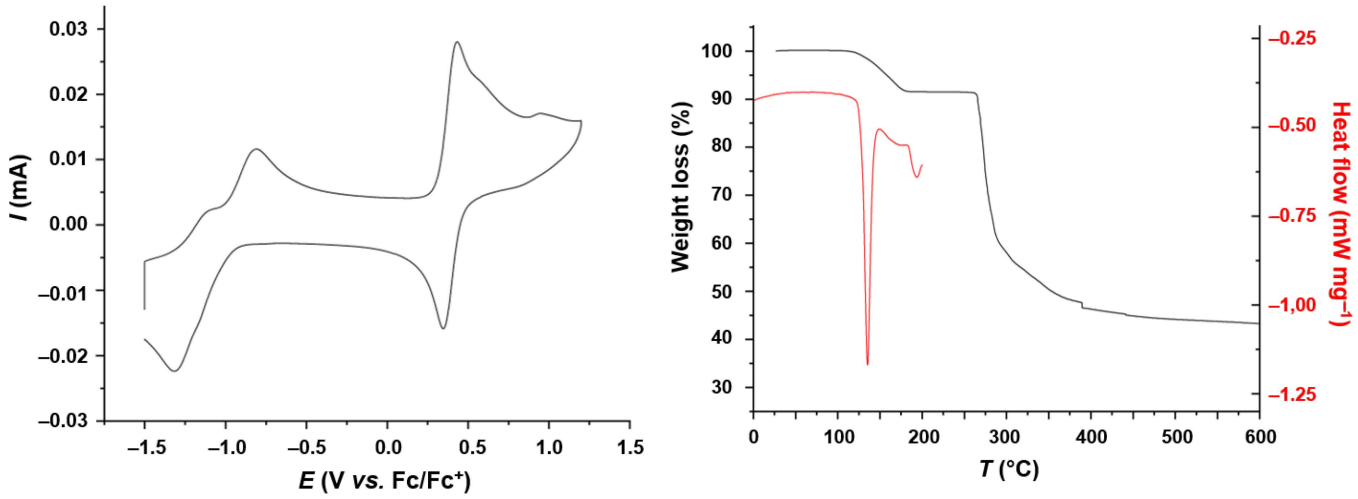

(**a**) (**b**)

Figure 4. (**a**) Cyclic voltammogram of **1** measured at room temperature in degassed CH_3CN containing 0.1 M $TBAPF_6$ (scan rate of 100 mV s^{-1}). (**b**) Thermal analysis of **1** by TGA (black curve) and DSC (red curve); the measurements were conducted under N_2 atmosphere with a heating rate of 20 K min^{-1}.

The thermal properties of **1** were analyzed by thermogravimetric analysis (TGA) and differential-scanning calorimetry (DSC). The combined TGA-DSC plot is shown in Figure 4b. The first step in the TGA curve, corresponding to a weight loss of 8.65%, was mainly due to the loss of the solvent-of-crystallization. According to ^{1}H-NMR analysis, the sample contained ca. 2.1 eq. of DMAc molecules (i.e., theoretical weight loss of 8.94%, see Figure S5). On the other hand, XRD analysis revealed the presence of only 1.3 eq. of DMAc in the unit cell, which would amount to a theoretical weight loss of 5.74%. This discrepancy can be rationalized by the fact that XRD analysis does not take disordered solvent molecules into account; thus, the actual solvent content is underestimated by XRD, whilst ^{1}H-NMR spectroscopy and elemental analysis provide more realistic values for the content of residual solvent (or solvent of crystallization). This process was assigned to the endothermic peak in the DSC at ca. 135 °C. The second endothermic process at ca. 192 °C could be due to recrystallization of the POM after the loss of the solvents-of-crystallization. Owing to the instrument's routing settings, DSC analysis could not be performed beyond 200 °C; thus, processes associated with an eventual melting or thermal degradation could not be analyzed further. The most significant weight loss of 47.72%, which occurred in the temperature range from 270 to 550 °C, was due to the decomposition of the TBA cations. Since this weight loss was more expressed than the calculated one (39.27%), a partial disintegration of the POM itself could not be excluded. Both POMs, i.e., **1** and **2**, revealed similar onset values for thermal degradation (263 °C vs. 255 °C), thus indicating the negligible influence of the substituent on the onset of the thermal stability (i.e., H vs. Ph). However, the weight loss of **2** was less pronounced and afforded a residual mass of 70% at 600 °C; the residual mass of **1**, however, was only 43% at the same temperature (Figure S13).

3. Discussion and Conclusions

The one-pot synthesis under solvothermal reaction conditions, assisted by microwave irradiation, afforded **1** in the good yield of 73%. The hybrid POM **1** repre-

sents the so-far missing member of the family of Anderson–Evans POMs derived from 2-(hydroxymethyl)propane-1,3-diol, i.e., the derivative with a $\{MnMo_6O_{24}\}$ core. Owing to the paramagnetic nature of the central Mn(III) ions, remarkable features in the compound's ^{1}H-NMR became apparent. In addition to the characteristic shift of the signal of the methylene groups to 56.13 ppm, the signal of the methinyl protons was observed at –16.51 ppm. These significant downfield and upfield shifts are due to the influence of the central Mn(III) ion in the high-spin state. Its magnetic anisotropy affects the protons of the CH_2- and CH-groups in a different fashion, since the distance r between the Mn(III) center and the protons, as well as the angle θ between the vector from the Mn(III) ion to the proton and the principal axis of the magnetic anisotropy tensor, must be considered [39,40]. This relationship is referred to as the pseudo-contact shift (δ_{PC}, Equation (1)).

$$\delta_{PC} \propto (3\cos 2\theta - 1)/r^3 \quad (1)$$

Secondly, the Fermi-contact shift (δ_{PC}), which depends on the spin-density of the paramagnetic nucleus, is particularly strong regarding protons in close proximity. The overall paramagnetic shift is the sum of both contributions. However, the deconvolution of the individual contributions cannot be provided with the complex POM system at hand. Nonetheless, compound **1** is a unique example of a hybrid POM where ^{1}H-NMR signals at very high and very low fields have been observed.

Moreover, quantum chemical calculations verified the assumption that the central Mn(III) was in its quintet high-spin state (S = 2). This scenario is reflected by coordination geometry and the bond lengths, as determined by scXRD analysis of **1**. This analysis of **1** also confirmed the highly symmetrical structure of the POM and the presence of three symmetry-independent polyoxoanions per unit cell. This represents an unusual feature which has seldomly been observed in hybrid Anderson–Evans-type POMs [17]. In comparison to the solid-state structure of **2** [14], the polyoxoanions of **1** were not interacting via *H*-bonding and ππ-stacking. The absence of these non-covalent interactions results in decreased stability, as reflected by the more pronounced thermal degradation of **1** upon heating up to 600 °C.

The electrochemical analysis of **1** revealed a decent redox stability in CH_3CN solution regarding both oxidation and reduction. Redox stability is beneficial for both potential applications: the HER in the presence of a potential sensitizer (e.g., Ir(III) or Ru(II) polypyridyl complexes) and energy storage. As previously mentioned, POMs have already been utilized as active materials in aqueous or non-aqueous RFBs—symmetric as well asymmetric ones [41]. In this broader context, compounds **1** and **2** are also of interest. Taking the molar mass of **1** into account, an anion-based theoretical capacity of 24 mAh g^{-1} can be deduced, which is comparable to those reported for other POM-based active materials [24]. The use of **1** as an HER catalyst and energy-storage material is subject of ongoing research.

4. Materials and Methods

4.1. General

All reagents and solvents (HPLC grade) were purchased from commercial suppliers (TCI, Eschborn, Germany) and used as received. The (n-Bu_4N)$_4$[α-Mo_8O_{26}] was synthesized from MoO_3 and (n-Bu_4N)OH according to the optimized protocol reported by Ikegami and Yagasaki [30]. The microwave-assisted reaction was performed in a capped microwave vial (5 mL) using a Biotage Initiator-8 microwave synthesizer (Uppsala, Sweden) (max. power of 400 W, working frequency of 4.45 GHz). The synthesis of **2** from (n-Bu_4N)$_4$[α-Mo_8O_{26}], $Mn(OAc)_3$, and 2-(hydroxymethyl)-2-phenylpropane-1,3-diol ("Ph-triol") has

been previously described [14]. The ^{1}H-NMR spectroscopic data were in full agreement with those reported earlier.

Fourier-transform infrared (FT-IR) spectra were recorded on a Shimadzu IR-Affinity-1 instrument in ATR mode (Duisburg, Germany). The intensity of bands is categorized as follows: weak (w), medium (m), strong (s), and very strong (vs).

The elemental analysis (CHNS) was carried out on a CHN-932 Automat Leco instrument (St Joseph, MI, USA).

Matrix-assisted laser desorption/ionization time-of-flight (MALDI-TOF) mass spectrometry measurements were carried out on a Bruker-Daltroics rapifleX MALDI-TOF/TOF System (Karlsruhe, Germany) equipped with a scoutMTP-II ion source and a smartbeam™ 3D laser (355 nm wavelength). Samples were prepared by the dried-droplet technique. The spectra were acquired in positive reflector mode using 9-aminoacridine (9-AA) or *trans*-2-[3-(4-*tert*-butylphenyl)-2-methyl-2-propenylidene]malononitrile (DCTB) with KCl as the matrix. The evaluation and processing of the recorded spectra were performed using the manufacturer's software flexAnalysis 4.0, including baseline subtraction and external calibration by Bruker's fleXstandard kit.

NMR experiments were performed on a Bruker Avance IV (NEO) 500 MHz spectrometer equipped with a nitrogen-cooled 5 mm 'Prodigy' BBO probe. Samples were measured in d_6-DMSO from Euriso-Top GmbH (Saarbrücken, Germany). Chemical shifts are reported in ppm, referenced to the residual solvent signal. For determination of longitudinal relaxation time (T1), an inversion recovery sequence with a recycle delay of 5 s was applied. The ^{1}H NMR spectra of the paramagnetic compound were acquired for a spectral width of 200 ppm using standard sequences. For the processing and analysis of the NMR spectra, the web-based NMRium software was used [42,43].

The X-ray powder diffractogram was recorded at room temperature in a capillary using a STOE Stadi-P diffractometer (Darmstadt, Germany) equipped with a Cu-Kα fine-focus X-ray source, which was operated at 40 kV and 40 mA in the Debye–Scherrer mode, and a Dectris Mythen 1K detector. Data were collected from 0 to 50° (2θ) with a step size of 2.1 and a time/PSD of 20 s.

Cyclic voltammetry (CV) measurements were performed using a BioLogic SAS VMP3 potentiostat (Göttingen, Germany). The measurement setup comprised a platin wire as a counter electrode, $Ag/AgNO_3$ as a reference electrode, and glassy carbon as a working electrode. The measurements were conducted in CH_3CN containing 0.1 M $TBAPF_6$. Potentials were calibrated against the Fc/Fc^+ redox couple (E = 0.39 V vs. Ag/Ag^+).

For the thermogravimetric analysis (TGA), a NETZSCH TG 209F1 Libra instrument was used (Selb, Germany). The measurement was performed under N_2 atmosphere in the range from room temperature to 1000 °C, with a heating rate of 20 K min^{-1}. Differential-scanning calorimetry (DSC) was performed on a NETZSCH DSC 204F1 Phoenix instrument (Selb, Germany). The measurement was carried out in the range from –50 to 200 °C under N_2-atosphere, with a heating rate of 20 K min^{-1}. The results of the TGA and SC measurements were analyzed using the Proteus-80 software provided by NETZSCH (Selb, Germany).

4.2. Synthesis of ***1***

A 10 mL microwave vial was equipped with $(TBA)_4[Mo_8O_{26}]$ (77.5 mg, 0.036 mmol), Mn(III) acetate dihydrate (14.5 mg, 0.054 mmol), 2-hydroxymethylpropan-1,3-diol (12.6 mg, 0.126 mmol), and *N*,*N*-dimethylacetamide (DMAc, 5 mL). The capped vial was heated for 3 h at 110 °C under microwave irradiation. The orange solution was cooled to room temperature and filtered to remove a fine white solid. Diffusion of diethyl ether into the filtrate yielded pale orange crystals (73% yield).

IR (ATR): 2957 (w), 2932 (w), 2870 (w), 1468 (w), 1462 (w), 1379 (w), 1043 (m), 939 (s), 914 (s), 899 (s), 874 (s), 752 (m), 739 (m), 648 (vs), 561 (s), 473 (s), 409 (s) cm^{-1}.

^{1}H-NMR (500 MHz, d_6-DMSO) δ_H 56.13 ppm (brs, 12H), 3.16 (m, 24H), 1.58 (m, 24H), 1.31 (m, 24H), 0.94 (m, 36H), –16.51 (brs, 2H) ppm.

^{13}C-NMR (125 MHz, d_6-DMSO) δ_C 58.0, 23.6, 19.8, 14.2 ppm (the signals of the organic ligand on the POM were not observed).

MALDI-TOF MS: m/z calcd. for $C_{72}H_{157}MnMo_6N_4O_{24}$ 2094.702, found 2094.486.

Elem. Anal. calcd. for $[C_{56}H_{122}MnMo_6N_3O_{24}] \times [C_4H_9NO]_{2\cdot2} \times [C_4H_{10}O]_{0\cdot8}$ C 38.88, H 7.20, N 3.33; found C 38.74, H 7.35, N 3.41.

4.3. X-Ray Diffraction Analysis of ***1***

The intensity data for compound **1** were collected on a Bruker Nonius KappaCCD diffractometer (Karlsruhe, Germany) (using graphite-monochromated Mo-K_α radiation. Data were corrected for Lorentz and polarization effects; absorption was considered on a semi-empirical basis using multiple scans [44–46]. The structure was solved by intrinsic phases (SHELXT [47]) and refined by full-matrix least-squares techniques against Fo^2 (SHELXL-2018 [48]). The hydrogen atoms were included at calculated positions with fixed thermal parameters. All non-hydrogen atoms were refined anisotropically [48]. Disordered moieties of the TBA cations were refined using displacement parameter restraints. The crystal of **1** contains large voids, filled with disordered solvent molecules. The void's size is 613 $Å^3$ per unit cell. Their contribution to the structure factors was secured by back-Fourier transformation using the SQUEEZE routine of the PLATON software [49], resulting in 206 electrons per unit cell. The structure representations were generated with the Mercury software package, version 2022.3.0 [50].

4.4. Computational Studies

All quantum chemical calculations were performed using the Gaussian 16(C.02) software package [51] in order to investigate structural and electronic properties of the Anderson–Evans POM **1** in the absence of the TBA cations. The fully relaxed equilibrium structure of the polyoxoanion of **1** were obtained considering three electronic scenarios, i.e., the (closed-shell or low-spin) singlet ground state (^{1}[**1**]$^{3-}$) as well as two (opened-shell) high-spin species—the triplet and quintet ground states (i.e., ^{3}[**1**]$^{3-}$ and ^{5}[**1**]$^{3-}$, respectively). For this purpose, initial structural properties were extracted from our previous joint synthetic-spectroscopic-theoretical investigation on the photophysical properties of a BODIPY-decorated Anderson–Evans-type POM [12]. The B3LYP exchange-correlation functional [52,53] was applied in combination with the all-electron def2-SVP basis set [54]. All structures were fully optimized without any symmetry restrictions within the gas phase as well as within CH_3CN. To this aim, implicit solvent effects (CH_3CN: ε = 35.688, n = 1.344) were considered by the solute electron density (SMD) variant of the integral equation formalism of the polarizable continuum model (equilibrium procedure) [55,56]. All calculations were performed, including D3 dispersion correction with Becke–Johnson damping [57]. Subsequently, a vibrational analysis was carried out for each optimized ground state structure (i.e., ^{1}[**1**]$^{3-}$, ^{3}[**1**]$^{3-}$, and ^{5}[**1**]$^{3-}$, in gas phase and in CH_3CN) to verify that a minimum on the 3N-6-dimensional potential energy (hyper-)surface (PES) was obtained. Finally, Boltzmann factors (at T = 298 K) were calculated based on the respective Gibbs energies of triplet and quintet species; the significantly less stable closed-shell species, ^{1}[**1**]$^{3-}$, was not considered.

Supplementary Materials: The following supporting information can be downloaded at: https://www.mdpi.com/article/10.3390/inorganics13080254/s1, Figure S1a: FT-IR spectrum of **1**; Figure S1b: FT-IR spectrum of **2**; Figures S2 and S3: MALDI-TOF mass spectra of **1**; Figures S4 and S5: ^{1}H-NMR

spectra of **1**; Figures S6 and S7: *T*1 relaxation measurements of **1**; Figure S8: DEPT-135 NMR spectrum of **1**, Figure S9: Solid-state structure of **1** showing the numbering scheme; Figure S10: Solid-state structure of **1** showing the *H*-bonding in the crystal structure; Figure S11: Representation of the packing of the TBA cations and polyoxoanions of **1** in the crystal lattice; Figure S12: Measured and calculated PXRD patterns of **1**; Figure S13: Thermogravimetric analysis of **1** and **2**; Table S1: Results of the *T*1 relaxation measurements of **1**. Table S2: Full list of the bond lengths and bond angles for **1**. Table S3: Relative electronic energies of the singlet, triplet) and quintet states of **1** in the gas phase. Table S4: Relative electronic energies of the singlet, triplet) and quintet states of **1** in CH_3CN solution.

Author Contributions: Conceptualization, A.W.; methodology, A.W.; formal analysis, A.W., N.E.S. and H.G.; investigation, P.E. and N.S.; computational studies, S.K.; resources, U.S.S.; data curation, A.W., N.E.S. and H.G.; writing—original draft preparation, A.W., N.E.S. and H.G.; writing—review and editing, U.S.S.; visualization, A.W.; supervision, U.S.S.; project administration, U.S.S.; funding acquisition, S.K. and U.S.S. All authors have read and agreed to the published version of the manuscript.

Funding: Financial support by the Deutsche Forschungsgemeinschaft (DFG) within the Priority Program "Light-controlled reactivity of metal complexes" (SPP-2102, LCRMC, project number 493768838) and the Collaborative Research Center TRR-234 ("CataLight"; projects A4, B2 and B9) is kindly acknowledged. Moreover, the DFG supported the acquisition of the 500 MHz NMR spectrometer (grant number INST 275/442-1 FUGG).

Institutional Review Board Statement: Not applicable.

Informed Consent Statement: Not applicable.

Data Availability Statement: Crystallographic data (excluding structure factors) for compound **1** has been deposited with the Cambridge Crystallographic Data Center (CCDC deposition number: 2226003). Copies of the data can be obtained free-of-charge on application to CCDC, 12 Union Road, Cambridge CB2 1EZ, UK (deposit@ccdc.cam.ac.uk; www.ccdc.cam.ac.uk, accessed on 20 May 2025). The whole dataset related to the content of this article is available on request from the authors. All optimized equilibrium structures as well as spin density cube-files of investigated opened-shell species (triplet and quintet) are freely available via Zenodo (https://doi.org/10.5281/zenodo.15691461).

Acknowledgments: The authors thank Nicole Fritz (MALDI-TOF MS), Sandra Köhn (elemental analysis), Antje Wermann (PXRD), and Renzo Paulus (TGA & DSC) for performing the respective measurements. Further thanks go to Phil Köhler for his support in visualizing the solid-state structure of **1**.

Conflicts of Interest: Patrick Endres was employed by the company evety GmbH c/o OGE. The remaining authors declare that the research was conducted in the absence of any commercial or financial relationships that could be construed as a potential conflict of interest.

References

1. Keggin, J.F. Structure of the molecule of 12-phosphotungstic acid. *Nature* **1933**, *131*, 908–909. [CrossRef]
2. Dolbecq, A.; Dumas, E.; Mayer, C.R.; Mialane, P. Hybrid organic–inorganic oolyoxometalate compounds: From structural diversity to applications. *Chem. Rev.* **2010**, *110*, 6009–6048. [CrossRef] [PubMed]
3. Wang, C.; Wang, B.; Yang, H.; Wan, Y.; Fang, H.; Bao, W.; Wang, W.; Wang, N.; Lu, Y. A review on polyoxometalates-based materials in addressing challenges faced by electrochemical energy storage systems. *Chem. Eng. J.* **2024**, *483*, 149143. [CrossRef]
4. Woźniak Budych, M.J.; Staszak, K.; Bajek, A.; Pniewski, F.; Jastrząb, R.; Staszak, M.; Tylkowski, B.; Wieszczycka, K. The future of polyoxymetalates for biological and chemical apllications. *Coord. Chem. Rev.* **2023**, *493*, 215306. [CrossRef]
5. Anyushin, A.V.; Kondinski, A.; Parac-Vogt, T.N. Hybrid polyoxometalates as post-functionalization platforms: From fundamentals to emerging applications. *Chem. Soc. Rev.* **2020**, *49*, 382–432. [CrossRef]
6. Lu, M.; Wei, Y.; Xu, B.; Cheung, C.F.-C.; Peng, Z.; Powell, D.R. Hybrid molecular dumbbells: Bridging polyoxometalate clusters with an organic π-conjugated rod. *Angew. Chem. Int. Ed.* **2002**, *41*, 1566–1568. [CrossRef]
7. Wang, L.-S.; Lu, Y.; Máille, G.M.Ó.; Anthony, S.P.; Nolan, D.; Draper, S.M. Sonogashira cross-coupling as a route to tunable hybrid organic–inorganic rods with a polyoxometalate backbone. *Inorg. Chem.* **2016**, *55*, 9497–9500. [CrossRef]

8. Zhu, L.; Zhu, Y.; Meng, X.; Hao, J.; Li, Q.; Wei, Y.; Lin, Y. DCC-Assisted esterification of a polyoxometalate-functionalized phenol with carboxylic acids. *Chem. Eur. J.* **2008**, *14*, 10923–10927. [CrossRef]
9. Bareyt, S.; Piligkos, S.; Hasenknopf, B.; Gouzerh, P.; Lacôte, E.; Thorimbert, S.; Malacria, M. Highly efficient peptide bond formation to functionalized Wells-Dawson-type polyoxotungstates. *Angew. Chem. Int. Ed.* **2003**, *42*, 3404–3406. [CrossRef]
10. Marcoux, P.R.; Hasenknopf, B.; Vaissermann, J.; Gouzerh, P. Developing remote metal binding sites in heteropolymolybdates. *Eur. J. Inorg. Chem.* **2003**, *2003*, 2406–2412. [CrossRef]
11. Schönweiz, S.; Rommel, S.A.; Kübel, J.; Micheel, M.; Dietzek, B.; Rau, S.; Streb, C. Covalent photosensitizer–polyoxometalate-catalyst dyads for visible-light-driven hydrogen evolution. *Chem. Eur. J.* **2016**, *22*, 12002–12005. [CrossRef] [PubMed]
12. Cetindere, S.; Clausing, S.T.; Anjass, M.; Luo, Y.; Kupfer, S.; Dietzek, B.; Streb, C. Covalent linkage of BODIPY-photosensitizers to Anderson-type polyoxometalates using CLICK chemistry. *Chem. Eur. J.* **2021**, *27*, 17181–17187. [CrossRef] [PubMed]
13. Santoni, M.-P.; Pal, A.K.; Hanan, G.S.; Proust, A.; Hasenknopf, B. Discrete covalent organic–inorganic hybrids: Terpyridine functionalized polyoxometalates obtained by a modular strategy and their metal complexation. *Inorg. Chem.* **2011**, *50*, 6737–6745. [CrossRef]
14. Winter, A.; Endres, P.; Schröter, E.; Jäger, M.; Görls, H.; Neumann, C.; Turchanin, A.; Schubert, U.S. Towards covalent photosensitizer-polyoxometalate dyads-bipyridyl-functionalized polyoxometalates and their transition metal complexes. *Molecules* **2019**, *24*, 4446. [CrossRef]
15. Qin, Z.; Li, Q.; Huang, Y.; Zhang, J.; Li, G.; Wei, Y. Recent advances in controllable alkoxylation chemistry of Anderson-type polyoxometalates from synthetic strategies perspective. *Chin. Sci. Bull.* **2018**, *63*, 3263. [CrossRef]
16. Zhang, J.; Huang, Y.; Li, G.; Wei, Y. Recent advances in alkoxylation chemistry of polyoxometalates: From synthetic strategies, structural overviews to functional applications. *Coord. Chem. Rev.* **2019**, *378*, 395–414. [CrossRef]
17. Blazevic, A.; Rompel, A. The Anderson–Evans polyoxometalate: From inorganic building blocks *via* hybrid organic–inorganic structures to tomorrows "Bio-POM". *Coord. Chem. Rev.* **2016**, *307*, 42–64. [CrossRef]
18. Wu, P.; Wang, Y.; Huang, B.; Xiao, Z. Anderson-type polyoxometalates: From structures to functions. *Nanoscale* **2021**, *13*, 7119–7133. [CrossRef]
19. Yan, Y.; Wang, H.; Li, B.; Hou, G.; Yin, Z.; Wu, L.; Yam, V.W.W. Smart self-assemblies based on a surfactant-encapsulated photoresponsive polyoxometalate complex. *Angew. Chem. Int. Ed.* **2010**, *49*, 9233–9236. [CrossRef]
20. Yan, Y.; Li, B.; He, Q.; He, Z.; Ai, H.; Wang, H.; Yin, Z.; Wu, L. Synthesis and redox-responsive self-assembly of ferrocene grafted Anderson-type polyoxometalate hybrid complexes. *Soft Matter* **2012**, *8*, 1593–1600. [CrossRef]
21. Li, X.-X.; Wang, Y.-X.; Wang, R.-H.; Cui, C.-Y.; Tian, C.-B.; Yang, G.-Y. Designed assembly of heterometallic cluster organic frameworks based on Anderson-type polyoxometalate clusters. *Angew. Chem. Int. Ed.* **2016**, *55*, 6462–6466. [CrossRef]
22. Hagen, T. Formation of Enantiomer-Uniform Tris(hydroxymethyl)methane Derivatives. Ph.D. Thesis, Dortmund University, Dortmund, Germany, 2000.
23. Cheng, M.; Xiao, Z.; Yu, L.; Lin, X.; Wang, Y.; Wu, P. Direct syntheses of nanocages and frameworks based on Anderson-type polyoxometalates *via* one-pot reactions. *Inorg. Chem.* **2019**, *58*, 11988–11992. [CrossRef] [PubMed]
24. Liu, Y.; Zhang, J.; Lu, S.; Xiang, Y. Polyoxometalate-based electrolyte materials in redox flow batteries: Current trends and emerging opportunities. *Mater. Rep. Energy* **2022**, *2*, 100094. [CrossRef]
25. Sun, P.; Gu, Y.; You, W.; Tan, Z. Studies on an iron heteropolyacid redox flow battery. *J. Electrochem.* **1997**, *3*, 71. [CrossRef]
26. Zhao, M.; Liu, Q.; Feng, Y.; Lv, H. Recent advances in polyoxometalate-based catalysts for light-driven hydrogen evolution. *Dalton Trans.* **2024**, *53*, 18083–18088. [CrossRef]
27. Zeb, Z.; Huang, Y.; Chen, L.; Zhou, W.; Liao, M.; Jiang, Y.; Li, H.; Wang, L.; Wang, L.; Wang, H.; et al. Comprehensive overview of polyoxometalates for electrocatalytic hydrogen evolution reaction. *Coord. Chem. Rev.* **2023**, *482*, 215058. [CrossRef]
28. Streb, C. New trends in polyoxometalate photoredox chemistry: From photosensitisation to water oxidation catalysis. *Dalton Trans.* **2012**, *41*, 1651–1659. [CrossRef]
29. Zhang, M.; Li, H.; Zhang, J.; Lv, H.; Yang, G.-Y. Research advances of light-driven hydrogen evolution using polyoxometalate-based catalysts. *Chin. J. Catal.* **2021**, *42*, 855–871. [CrossRef]
30. Ikegami, S.; Yagasaki, A. Efficient syntheses of $[(n\text{-}C_4H_9)_4N]_4[\alpha\text{-}Mo_8O_{26}]$ and $[(n\text{-}C_4H_9)4N]_2[Mo_2O_7]$. *Materials* **2009**, *2*, 869–875. [CrossRef]
31. Hasenknopf, B.; Delmont, R.; Herson, P.; Gouzerh, P. Anderson-type heteropolymolybdates containing *tris*(alkoxo) ligands: Synthesis and structural characterization. *Eur. J. Inorg. Chem.* **2002**, *2002*, 1081–1087. [CrossRef]
32. Boulicault, J.E.; Alves, S.; Cole, R.B. Negative ion MALDI mass Spectrometry of polyoxometalates (POMs): Mechanism of singly charged anion formation and chemical properties evaluation. *J. Am. Soc. Mass Spectrom.* **2016**, *27*, 1301–1313. [CrossRef]
33. Gumerova, N.I.; Rompel, A. Polyoxometalates in solution: Speciation under spotlight. *Chem. Soc. Rev.* **2020**, *49*, 7568–7601. [CrossRef] [PubMed]
34. Lin, C.-G.; Hutin, M.; Busche, C.; Bell, N.L.; Long, D.-L.; Cronin, L. Elucidating the paramagnetic interactions of an inorganic–organic hybrid radical-functionalized Mn-Anderson cluster. *Dalton Trans.* **2021**, *50*, 2350–2353. [CrossRef]

35. Song, Y.-F.; Long, D.-L.; Cronin, L. Hybrid polyoxometalate clusters with appended aromatic platforms. *CrystEngComm* **2010**, *12*, 109–115. [CrossRef]
36. Tian, A.-x.; Ying, J.; Peng, J.; Sha, J.-q.; Pang, H.-j.; Zhang, P.-p.; Chen, Y.; Zhu, M.; Su, Z.-m. Tuning the dimensionality of the coordination polymer based on polyoxometalate by changing the spacer length of ligands. *Cryst. Growth Des.* **2008**, *8*, 3717–3724. [CrossRef]
37. Kupfer, S. Quantum chemical data: A missing member of the Anderson-Evans family: Synthesis and characterization of the trimethylolmethane-capped $\{MnMo_6O_{24}\}$ cluster. *Zenodo* **2025**. [CrossRef]
38. Schönweiz, S.; Heiland, M.; Anjass, M.; Jacob, T.; Rau, S.; Streb, C. Experimental and theoretical investigation of the light-driven hydrogen evolution by polyoxometalate–photosensitizer dyads. *Chem. Eur. J.* **2017**, *23*, 15370–15376. [CrossRef]
39. Novotny, J.; Komorovsky, S.; Marek, R. Paramagnetic effects in NMR spectroscopy of transition-metal complexes: Principles and chemical concepts. *Acc. Chem. Res.* **2024**, *57*, 1467–1477. [CrossRef]
40. Ravera, E.; Gigli, L.; Fiorucci, L.; Luchinat, C.; Parigi, G. The evolution of paramagnetic NMR as a tool in structural biology. *Phys. Chem. Chem. Phys.* **2022**, *24*, 17397–17416. [CrossRef]
41. Han, M.; Sun, W.; Hu, W.; Liu, Y.; Chen, J.; Zhang, C.; Li, J. Emerging polyoxometalate clusters-based redox flow batteries: Performance metrics, application prospects, and development strategies. *Energy Storage Mater.* **2024**, *71*, 103576. [CrossRef]
42. NMRium: NMR Spectra Processing for Everybody. Available online: www.nmrium.org (accessed on 15 June 2025).
43. Patiny, L.; Musallam, H.; Bolaños, A.; Zasso, M.; Wist, J.; Karayilan, M.; Ziegler, E.; Liermann, J.C.; Schlörer, N.E. NMRium: Teaching nuclear magnetic resonance spectra interpretation in an online platform. *Beilstein J. Org. Chem.* **2024**, *20*, 25–31. [CrossRef] [PubMed]
44. Hooft, R.W.W. COLLECT—Data Collection Software. Nonius B.V.: Delft, The Netherlands, 1998.
45. Otwinowski, Z.; Minor, W. Processing of X-Ray Diffraction Data Collected in Oscillation Mode. In *Methods in Enzymology, Vol. 276, Macromolecular Crystallography (Part A)*; Carter, C.W., Sweet, R.M., Eds.; Academic Press: London, UK, 1997; pp. 307–326.
46. Sheldrick, G.M. SADABS—Version 2.10. University of Göttingen: Göttingen, Germany, 2002.
47. Sheldrick, G.M. SHELXT—Integrated space-group and crystal-structure determination. *Acta Cryst. Sect. A* **2015**, *71*, 3–8. [CrossRef]
48. Sheldrick, G.M. Crystal structure refinement with SHELXL. *Acta Cryst. Sect. C* **2015**, *71*, 3–8. [CrossRef]
49. Spek, A. PLATON SQUEEZE: A tool for the calculation of the disordered solvent contribution to the calculated structure factors. *Acta Cryst. Sect. C* **2015**, *71*, 9–18. [CrossRef]
50. Macrae, C.F.; Edgington, P.R.; McCabe, P.; Pidcock, E.; Shields, G.P.; Taylor, R.; Towler, M.; van de Streek, J. Mercury: Visualization and analysis of crystal structures. *J. Appl. Cryst.* **2006**, *39*, 453–457. [CrossRef]
51. Frisch, M.J.; Trucks, G.W.; Schlegel, H.B.; Scuseria, G.E.; Robb, M.A.; Cheeseman, J.R.; Scalmani, G.; Barone, V.; Petersson, G.A.; Nakatsuji, H.; et al. *Gaussian 16 (rev. C.02)*; Gaussian: Wallingford, CT, USA, 2016.
52. Becke, A.D. Density-functional thermochemistry. Part III. The role of exact exchange. *J. Chem. Phys.* **1993**, *98*, 5648–5652. [CrossRef]
53. Lee, C.; Yang, W.; Parr, R.G. Development of the Colle-Salvetti correlation-energy formula into a functional of the electron density. *Phys. Rev. B* **1988**, *37*, 785–789. [CrossRef]
54. Weigend, F.; Ahlrichs, R. Balanced basis sets of split valence, triple zeta valence and quadruple zeta valence quality for H to Rn: Design and assessment of accuracy. *Phys. Chem. Chem. Phys.* **2005**, *7*, 3297–3305. [CrossRef]
55. Marenich, A.V.; Cramer, C.J.; Truhlar, D.G. Universal Solvation Model Based on Solute Electron Density and on a Continuum Model of the Solvent Defined by the Bulk Dielectric Constant and Atomic Surface Tensions. *J. Phys. Chem. B* **2009**, *113*, 6378–6396. [CrossRef]
56. Mennucci, B.; Cappelli, C.; Guido, C.A.; Cammi, R.; Tomasi, J. Structures and Properties of Electronically Excited Chromophores in Solution from the Polarizable Continuum Model Coupled to the Time-Dependent Density Functional Theory. *J. Phys. Chem. A* **2009**, *113*, 3009–3020. [CrossRef]
57. Grimme, S.; Ehrlich, S.; Goerigk, L. Effect of the damping function in dispersion corrected density functional theory. *J. Comput. Chem.* **2011**, *32*, 1456–1465. [CrossRef]

Disclaimer/Publisher's Note: The statements, opinions and data contained in all publications are solely those of the individual author(s) and contributor(s) and not of MDPI and/or the editor(s). MDPI and/or the editor(s) disclaim responsibility for any injury to people or property resulting from any ideas, methods, instructions or products referred to in the content.